Journal of Materials Chemistry A

ARTICLE

Biotemplating: A Sustainable Synthetic Methodology for Na-ion Battery Materials†

Received 00th January 20xx,
Accepted 00th January 20xx

DOI: 10.1039/x0xx00000x

www.rsc.org/

Silvija Zilinskaite,[a] Anthony J. R. Rennie,[b] Rebecca Boston,*[a] Nik Reeves-McLaren*[a]

Dextran biotemplating is a novel, sustainable and reduced-temperature synthetic approach that allows a high level of control over the size and shape of particles formed. This article discusses the application of this technique to the synthesis of an important candidate sodium-ion positive electrode material, $Na_{2/3}Ni_{1/3}Mn_{2/3}O_2$ (or 'NNM'), with a high theoretical specific capacity (173 mAh g^{-1}). While a solid state reference sample prepared at 850 °C exhibited a specific capacity of ~80 mAh g^{-1} after 10 cycles, samples made *via* our dextran biotemplating route with final calcination at 550 °C for 12 h showed a large and significant improvement at 103.1 mAh g^{-1}, under the same operating conditions.

Introduction

To reduce society's reliance on fossil fuels and lower carbon emissions, the electricity grids of the future are likely to move increasingly towards decentralisation and reliance on renewable sources such as wind, wave, and solar power. Given the intermittency of such sources, to manage fluctuations in energy production and consumption it is essential that efficient large-scale stationary energy storage systems are developed to allow decoupling of supply and demand.

Energy storage systems based on Li-ion battery (LIB) technology are well established for small scale and portable devices and have become ubiquitous in modern life. They are also receiving research attention for such grid-scale applications. However, given the relative scarcity and high cost of Li-containing ores, and the ongoing safety concerns and limited cycle life of LIB cells, it is clear that alternative systems must be investigated urgently. Sodium-ion batteries (NIBs) present an alternative of real potential: Na is cheaper and far more abundant than Li. NIBs can be stored safely at 0 V, and have the potential to show improved cycle life. To deliver on their promise, however, the development of high energy density cathode materials is essential.

Sodium-ion cathode materials for NIBs have received significant research attention, but remain far less developed than their lithium-based cousins. Four main families of materials are under investigation: (i) layered sulfides;[1] (ii) fluoride perovskites;[2] (iii) polyanionic species, such as phosphates[3–5] and sulphates[6]; and (iv) oxides,[7] including layered transition metal oxides (LTMOs) such as $Na_{2/3}Ni_{1/3}Mn_{2/3}O_2$ (or 'NNM'), which has attracted much interest due to its high theoretical specific capacity (173 mAh g^{-1}) and good cycling performance. Observed experimental discharge capacities for NNM vary widely depending on the precise voltage range and charge rate used, but are typically ~80 mAh g^{-1} for cells cycled between 2 and 4 V.[8–10] Extending the operating voltage range greatly improves first discharge capacities but leads to significant losses on cycling.

NNM crystallises in a number of different polymorphs, generally consisting of edge-sharing octahedral units forming $(Mn_{2/3}Ni_{1/3}O_2)_n$ layers, with Na^+-ions residing between layers. The polymorphs are classified according to the scheme proposed by Delmas *et al.*,[11] with a label based on (i) the Na-ion coordination environment, with octahedral (O-type), tetrahedral (T-type) and prismatic (P-type) arrangements common, followed with (ii) a number representing the number of transition metal layers per unit cell. Commonly reported polymorphs of NNM are O3 (*i.e.* indicating that Na is octahedrally-coordinated, with three metal layers per unit cell), P2 and P3.

The P2 and O3 polymorphs tend to form most readily at the high reaction temperatures used in most studies of NNM-related compounds, with higher Ni^{2+} contents leading to preferential formation of O3, and larger Mn^{4+} concentrations favouring P2. These polymorphs exhibit moderately different electrochemistry as a result of their differing crystal structures;[12] in O3 phases, Na^+ ions must migrate *via* an intermediate face-sharing tetrahedral site, which limits the diffusion rate and lowers rate capability. P2-based materials have a more direct Na^+-ion conduction pathway, and consequently show improved rate performance. Komaba *et al.* highlight the poor reversibility when charging O3 phases above 4.0 V.[13] While P2 and O3 are well studied, there are relatively few studies of P3-NNM phases. One major concern with all polymorphs is that electrochemical activity is exhibited across multiple charge plateaus over wide voltage windows, often

[a] Department of Materials Science and Engineering, University of Sheffield, Sheffield, S1 3JD, UK.
[b] Department of Chemical and Biological Engineering, University of Sheffield, Sheffield, S1 3JD, UK.

† Electronic Supplementary Information (ESI) available. See DOI: 10.1039/x0xx00000x

from *e.g.* 1.5 to 4.5 V. This is not well suited for applications, and optimisation is required.

A recent investigation[10] focussed on the behaviour of P2- and P3-NNM produced *via* spray pyrolysis at 800 °C; the latter transformed to P2 on subsequent calcination above 700 °C. When cycled in the potential range of 2.0 - 4.0 V, P2- and P3-NNM display subtly different behaviour with distinct double peaks observed in cyclic voltammograms for P3-NNM (and little capacity delivered below 3.0 V) and more discrete peaks seen on cycling P2-NNM. Peaks above 3.0 V for both P2 and P3 were attributed to the Ni^{2+}/Ni^{3+} and Ni^{3+}/Ni^{4+} redox couples; for P2, activity at *ca.* 2.5 V was attributed to Mn^{3+}/Mn^{4+}. Overall discharge capacities were modest; P3-NNM showed a first cycle discharge capacity of 62 mAh g^{-1} and P2 exhibiting 69-86 mAh g^{-1}, depending on calcination temperature.

Some studies have sought to optimise the electrochemistry of LTMOs by preparing composite materials, with *e.g.* P2/O3 intergrowth structures in Mg,Fe-doped NNM.[12,14] Such approaches show great promise, with synergistic effects resulting in specific discharge capacities of up to 155 mAh g^{-1}, high average discharge potentials (3.4 V *vs* Na/Na^+), coulombic efficiencies over 99.9%, and good capacity retention over hundreds of cycles.[12]

A range of synthetic approaches have been reported for LTMO cathode materials for NIBs, *e.g.* solid state reaction,[9,12] combustion[15] and sol-gel syntheses,[16] and spray pyrolysis.[10] Most studies involve a final long duration high temperature (>800 °C) reaction stage and pay little attention to the sustainability of the materials or synthetic approach used, or to powder processability and the targeted fabrication of specific particle sizes or morphologies. There has been negligible attention on the role particle morphology might play in optimising electrochemical performance. With NIBs a nascent technology, it is timely that (i) alternative sustainable approaches be investigated to identify synthetic methods with lower economic and environmental costs, and (ii) the impact of particle morphology on cell performance be elucidated. As has been shown with $LiFePO_4$,[17] nanoscaling can make significant improvements to electrochemical efficiency, by creating greater surface area to volume ratios and shorter diffusion distances. We propose that Na-ion cathode materials may benefit from a similar nanoscaling approach.

An ideal synthetic method for NIB materials would need to enable simultaneous fine control over stoichiometry and morphology, allowing for the fabrication of nanoscale materials, whilst addressing common sustainability issues[18] faced in large scale production, *e.g.* high energy consumption. One such method is biotemplating,[19] where biological and naturally occurring long chain polymeric molecules are used to control, constrain and direct crystal growth and stoichiometry[20] during synthesis. Biotemplates contain large numbers of functional groups (e.g. hydroxyls, carboxylates) which can be used to create negatively charged chelation sites when deprotonated in water. These chelation sites can be used to uptake metal cations from solution forming a homogeneously mixed organic/inorganic composite or gel. During heating, the organic component (biotemplate) prevents agglomeration of the forming intermediate materials or product. As the temperature is increased further, the template burns away completely, promoting formation of nano-sized crystallites whose morphology is dependent on template choice; often biotemplates produce nanopowders or foams,[20] but some produce complex polycrystalline macro-morphologies which directly replicate the initial shape of the template (*e.g.* the use of dextran spheres to create polycrystalline spheres of oxide superconductors).[21]

One of the most commonly used biotemplates is dextran, a glycosidic polymer consisting of an α1-6 backbone with α1-3 side chains, produced via bacterial digestion. It has become a popular choice for oxide syntheses as it produces reticulated and high surface area structures, often at reduced reaction times and temperatures compared to traditional solid state methods.[22] The majority of studies performed so far using dextran have been proofs-of-concept using model systems such as yttrium barium copper oxide, focussing on formation mechanisms[21] and morphology-function relationships, *e.g.* with high temperature superconductors, dextran templated samples showed significant improvements in critical current density, directly linked to the morphologies formed.[22]

Here, we demonstrate the use of dextran biotemplating in the synthesis of nanoscale NNM, and investigate links between particle size (as controlled by the biotemplate and heating protocol) and electrochemical performance. We show that electrochemical performance, in particular specific capacity, can be significantly improved through the control of crystallite size enabled by biotemplating. By closely controlling the heating protocol used, we show that biotemplating can be used to select the size of crystallites, creating oxide powders with targeted morphology-function relationships. Solid state analogues were synthesised for direct comparison, and highlight the significant impact which biotemplating can have on both the processing time/temperature and on functionality.

Experimental

All reagents were of 98+% purity, obtained from Sigma Aldrich (UK) and used without further purification. For the biotemplated specimens, stoichiometric solutions of sodium carbonate, nickel acetate and manganese acetate were dissolved in water and a small quantity of nitric acid added to aid dissolution. 10 wt.% dextran was added to the solutions and then samples were dried at 90 °C. Dried samples were then heated at 10 °C min^{-1} in a muffle furnace in air, and calcined at 550 °C, 650 °C, 750 °C or 850 °C for 2 h, 5 h, or 12 h. For comparison, an additional sample was prepared using standard 'solid state' processing methods, with sodium carbonate, nickel oxide and manganese oxide as reagents. Stoichiometric quantities of the starting compounds were weighed, ground in an agate mortar and pestle, then placed into an alumina crucible and heated, in a muffle furnace and air atmosphere, to 850 °C at 10 °C min^{-1}, and calcined for 12 h.[9]

X-ray diffraction (XRD) used a PANalytical X'Pert^3 Powder diffractometer with Ni-filtered Cu Kα radiation (λ = 1.5406 Å)

and a PIXcel[1D] detector. Phase analysis used the International Center for Diffraction Data's PDF-4+ database, 2016 edition, and Sleve+ software. Preliminary Rietveld refinements were conducted using the EXPGUI[23] interface for GSAS[24]; any errors quoted are as provided by GSAS. Initial isotropic thermal parameters, U_{iso}s, were set to 0.025 Å^2 for all crystallographic sites and constrained to be the same for shared Mn,Ni sites. The background was refined first, using a shifted Chebyshev function with 10 terms, followed by the lattice parameter(s) for the P2 and/or P3 phase(s), phase fraction scale factors and profile parameters, LX, to model peak broadening due principally to crystallite size effects. Significant preferred orientation effects for the P2 and/or P3 phases were observed in all datasets; data were fitted using an 8-term spherical harmonic (ODF) preferred orientation function. Finally, atomic positions in order of scattering factor and U_{iso}s for metal sites were refined. The process was repeated to convergence until there were negligible shifts in refined variables.

Mn and Ni K-edge XANES measurements were undertaken at beamline B18 at the Diamond Light Source, Harwell, U.K. This beamline covers a wide energy range (2.05–35 keV) and is equipped with a double-crystal monochromator containing two pairs of crystals, Si(111) and Si(311), optimized for quick EXAFS (QuEXAFS) measurements.[25] Spectra were collected in transmission mode with the intensities of the incident and transmitted X-ray beams measured using gas filled ionization chambers. Metal foils were placed in front of a third ionization chamber to allow the data to be corrected for any drift of the monochromator position and to permit accurate calibration of the energy scale in the XANES spectra. Three scans were collected for each sample; these were summed, calibrated, background subtracted, and normalized using the program Athena.[26] XANES spectra were measured for $Mn^{2+}CO_3$, $Mn^{2.67+}{}_3O_4$, $Mn^{3+}{}_2O_3$, $Mn^{4+}O_2$, $Ni^{2+}O$, and Ni^0 metal foil as oxidation state reference materials.

Samples for scanning electron microscopy (SEM) were prepared by affixing the powder to carbon tape and sputter-coating with a 15 nm layer of gold. Samples were then examined using a Phillips Inspect F SEM. Average crystallite sizes for each sample were obtained through manual measurement of a statistically significant number of crystallites using ImageJ.[27]

Nitrogen adsorption/desorption isotherms at -196 °C were collected using a Micromeritics 3Flex instrument; samples were degassed under vacuum at 200 °C for 10 h before analysis.

Electrodes were prepared by mixing 80 wt.% of the material under study, 10 wt.% PVdF binder and 10 wt.% carbon (Super C45, Imerys Graphite & Carbon) and dispersing with a sufficient volume of 1-methyl-2-pyrrolidone (anhydrous 99.5%, Sigma-Aldrich). The slurry was mixed thoroughly and cast onto carbon coated aluminium foil using a micrometer adjustable paint applicator. After drying under vacuum the sheets were calendared using a rolling mill until the coating thickness was *ca.* 70 µm. 12 mm diameter discs were punched from the sheet for use as electrodes and the active material loading was in the region of 3.20 - 5.40 mg cm^{-2}.

Stainless steel coin cells (2016) were assembled in an argon-filled glovebox (MBraun) by layering a stainless steel spacer, the cathode under study, a glass fibre separator (GF/F, Whatman) soaked in electrolyte solution, and a disc punched from freshly cut and rolled sodium ingot (99.8 %, Alfa Aesar). 1.0 mol l^{-1} electrolyte solution was prepared by dissolving sodium hexafluorophosphate (99+%, Alfa Aesar) into the appropriate volume of anhydrous diethylene glycol dimethyl ether (Sigma Aldrich) in an argon-filled glovebox. The solvent was stored over a 4 Å molecular sieve before use and the moisture content of the electrolyte solution was determined to be less than 20 ppm by Karl Fisher titration (899 Coulometer, Metrohm).

Electrochemical tests were performed at 25 °C in climatic chambers and cells were left under open circuit conditions for 8 h before cycling. Cathodes were cycled galvanostatically between 4.2 V and 2.0 V (*vs* Na/Na$^+$) at a rate of 10 mA g^{-1} using a Maccor Series 4000 Battery Cycler. Electrochemical testing was performed on at least two cells for each material to ensure reproducibility. (All subsequent references to potential and voltage are relative to the Na/Na$^+$ reference.)

Results and Discussion

Phase Analysis

Analysis of X-ray diffraction data was carried out on as-prepared specimens made *via* solid state reaction at 850 °C and biotemplating at 550 to 850 °C. The P2 and P3 polymorphs give broadly similar diffraction patterns, with peak overlaps common on many larger Bragg lines from the two phases. However, distinction can be made with care; the P2 phase exhibits some additional reflections, e.g. the (102) line at ~39.5 °2θ, not present in other polymorphs and some minor changes in relative peak intensities.

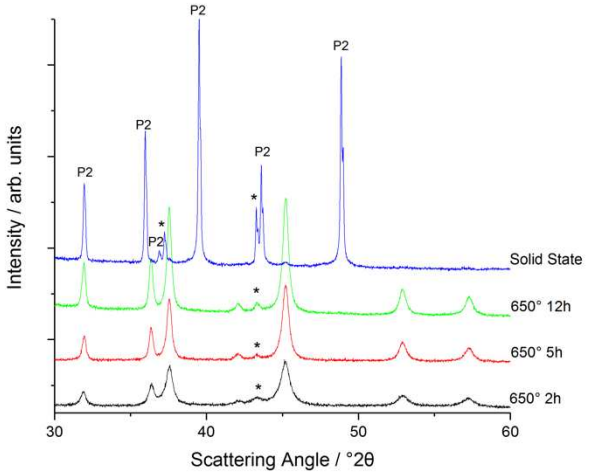

Figure 1. X-ray diffraction patterns collected at 22 °C for $Na_{2/3}Ni_{1/3}Mn_{2/3}O_2$ prepared by solid state synthesis at 850 °C, 12 h and *via* dextran biotemplating at 650 °C for 2, 5 and 12 h. Peaks are from the P3-NNM polymorph unless specifically and individually labelled (P2 = P2-NNM, * = NiO). For fully indexed diffraction patterns, see Supplementary Information.

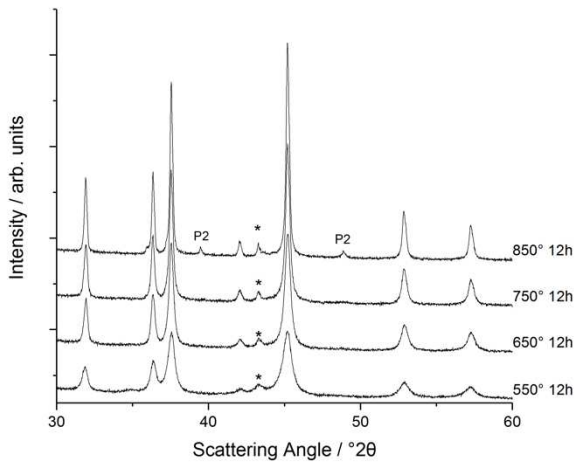

Figure 2. X-ray diffraction patterns collected at 22 °C for $Na_{2/3}Ni_{1/3}Mn_{2/3}O_2$ prepared by dextran biotemplating using a 12 h final calcination at 550 °C, 650 °C, 750 °C and 850 °C. Peaks are from the P3-NNM polymorph unless specifically and individually labelled (P2 = P2-NNM, * = NiO). For fully indexed diffraction patterns, see Supplementary Information, Figures S3a, and S3d-f.

For the sample made *via* solid state synthesis at 850 °C, the reflections observed, Figure 1, were largely indexed using the $P6_3/mmc$ space group commonly associated with the P2 polymorph of NNM, with refined lattice parameters of a = 2.88137 (9) Å, c = 11.1903 (7) Å. A small amount of an NiO-type phase was also noted; observation of small amounts of NiO-type secondary phases in the synthesis of NNM-related compositions, as found here, is not uncommon, and has been reported elsewhere in the literature.[9,10,12]

Samples made using the biotemplating methodology at 550 °C, 650 °C and 750 °C gave a mixture of P3-NNM and NiO, with peaks for the former indexing well against the R3m space group. In specimens reacted at 650 °C for 2 h, 5 h and 12 h, no significant shifts in Bragg line position or relative peak intensities were observed, Figures 1 and 2, suggesting that full reaction has been reached relatively quickly during calcination. However, some sharpening of the peaks can be observed, Figure 2, suggesting significant growth in crystallite size occurs with both increasing reaction time and/or temperature.

Similar observations can be noted in the data, Figure 2, for specimens fabricated at 850 °C, with the exception of two additional reflections emerging for the sample held at temperature for 12 h, which is due to the emergence of a small amount of the P2 polymorph.

Rietveld Refinement

Preliminary Rietveld refinements were conducted for materials prepared *via* both solid state and biotemplating synthetic methods using the crystal structures of the P2 and/or P3 polymorphs as reported by Dahn *et al.*[28] as starting points. In all cases, a secondary phase was added to account for the NiO-type phase ($Fm\bar{3}m$, initial lattice parameters a = 4.176 Å was added, with Ni on a 4*a* site, and O on the 4*b* site). After refinement of all appropriate parameters simultaneously, good visual fits were obtained for all refined datasets, and the lattice parameters and concentration of secondary phases

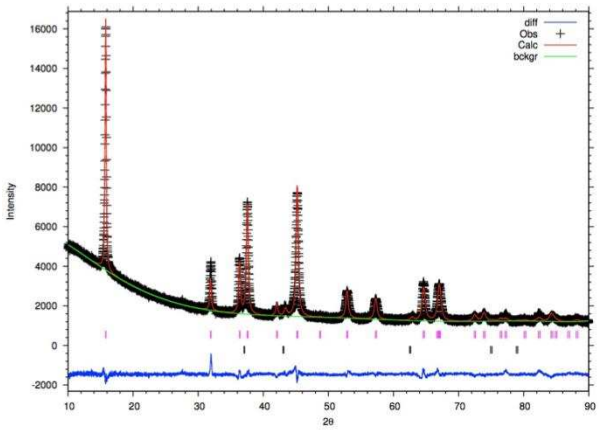

Figure 3. Observed, calculated and difference profiles from Rietveld refinements using GSAS+EXPGUI and room temperature XRD data for $Na_{2/3}Ni_{1/3}Mn_{2/3}O_2$ prepared by dextran biotemplating using a 12 h final calcination at 650 °C.

(NiO in all cases, and P2 in the case of the biotemplated sample heated at 850 °C, 12 h) are listed in Table 1.

As a representative example of a refinement, the (i) observed, calculated and difference profiles and (ii) final refined structural parameters for the biotemplated sample heated at 650 °C, 12 h are given in Figure 3 and Table 2, respectively. The visual fit is good, as were the various quality indicators: χ^2 = 2.84, R_{wp} = 5.11% and R_p = 3.72%. Refinement of reliable thermal parameters was difficult in part due to significant issues with preferred orientation in all datasets which resulted in poor fitting of those Bragg lines with large l components, e.g. the (004) and (103) reflections. It was not possible to refine sensible U_{iso}s for the two oxygen sites; this is likely explained by both the preferred orientation issues and the relatively weak X-ray scattering of the light oxygen atoms compared to the transition metals present. Further work is planned to include neutron diffraction and chemical analyses to more precisely characterise the crystal structures formed.

It was, however, straightforward to refine lattice parameters for the various specimens, Table 2. The a lattice parameter is relatively consistent and remains ~ 2.885 ± 0.003 Å regardless of synthesis time or temperature. The c parameter is more variable, with all specimens prepared at 550 °C and the sample prepared at 650 °C for 2 h showing relatively enlarged unit cells in the c axis. The reason for this is as yet unknown. Possible causes include: compositional variation and structural disorder, *e.g.* cations intermixing between the Na and Mn,Ni sites, though no evidence was seen for this in Rietveld fitting; partial reduction of the specimens as the carbon-rich biotemplate is burned off, with incomplete reoxidation occurring at lower calcination temperature/time combinations, though XANES data, see later, show no evidence to suggest formation of lower than anticipated average Mn,Ni oxidation states. Another possibility is that as the initial stages of dextran biotemplating are completed in an aqueous environment, it may be that at these lower calcination temperatures and times incomplete dehydration may be occurring, with some water molecules still residing within Na layers.

Table 1. Structural parameters, physical characteristics and electrochemical performance for solid state material and biotemplated $Na_{2/3}Ni_{1/3}Mn_{2/3}O_2$ prepared by dextran biotemplating and a range of calcination temperatures and durations. Data on calculated pore volumes are available in the Supplementary Information.

Calcination		Phases		Lattice Parameters[a]			Morphology		Electrochemistry			
Temp. /°C	Time /h	NNM polymorph(s)	NiO[a] /wt.%	a /Å	c /Å	V /Å^3	d_{av}[b] /nm	S_{BET}[c] /m^{2}g^{-1}	q_{c1}[d] / mAh g^{-1}	q_{d1}[e] / mAh g^{-1}	C.E.$_1$[f] /%	q_{d10}[g] / mAh g^{-1}
550	2	P3	7.3 (1)	2.9958 (2)	16.8706 (24)	121.67 (2)	102 (32)	108.0	n.d.	n.d.	n.d.	n.d.
	5	P3	13.6 (2)	2.8817 (2)	16.9157 (37)	121.65 (3)	108 (34)	127.7	n.d.	n.d.	n.d.	n.d.
	12	P3	6.2 (2)	2.8876 (1)	16.8690 (17)	121.81 (2)	124 (21)	52.9	121.1	108.5	89.6	103.1
650	2	P3	8.3 (2)	2.8856 (2)	16.8661 (25)	121.63 (2)	115 (25)	38.6	132.1	110.0	83.2	98.9
	5	P3	2.2 (2)	2.8869 (1)	16.8319 (13)	121.49 (1)	119 (32)	36.9	120.4	104.8	87.1	91.7
	12	P3	2.7 (1)	2.88437 (7)	16.8210 (10)	121.20 (1)	167 (41)	33.3	120.7	88.8	73.6	87.0
750	2	P3	1.4 (1)	2.88640 (6)	16.8239 (9)	121.39 (1)	193 (85)	38.4	178.2	108.0	60.6	83.8
	5	P3	1.1 (1)	2.88449 (6)	16.8230 (9)	121.22 (1)	263 (91)	27.4	n.d.	n.d.	n.d.	n.d.
	12	P3	3.3 (1)	2.88463 (5)	16.8176 (7)	121.19 (1)	309 (98)	31.6	122.1	109.9	90.0	86.8
850	2	P3	1.0 (1)	2.88418 (4)	16.8171 (6)	121.15 (1)	258 (73)	33.8	143.4	131.6	91.8	83.2
	5	P3	1.7 (1)	2.88492 (4)	16.8334 (6)	121.33 (1)	274 (118)	33.8	147.4	120.9	82.0	83.2
	12	P3 + 1.1 (1) wt.% P2	1.9 (1)	2.88374 (5)	16.8258 (5)	121.17 (1)	553 (253)	29.3	147.8	140.3	94.9	86.0
Solid state		P2	5.7 (3)	2.88137 (9)*	11.1903 (7)*	80.46 (1)*	1740 (742)	21.5	105.2	80.1	76.2	81.0

[a] as determined *via* Rietveld refinement using XRD data [b] average particle width determined *via* image analysis of SEM micrographs [c] specific surface area determined using nitrogen sorption [d] q_{d1} specific capacity of initial charge step [e] q_{c1} specific capacity of initial charge step [f] C.E.$_1$ coulombic efficiency of first cycle [g] q_{d10} specific capacity of 10th discharge step (n.d. not determined)

Table 2 Structural refinement parameters for $Na_{2/3}Ni_{1/3}Mn_{2/3}O_2$ specimen synthesised *via* dextran biotemplating with final calcination at 650 °C for 12 h. XRD data collected under ambient conditions. U_{iso}s for oxygens fixed at 0.025 Å^2

Parameter	Value
Space group	R3m
a / Å	2.88437 (7)
c / Å	16.8210 (10)
V / Å^3	121.20 (1)
χ^2	2.84
R_{wp} / %	5.11
R_p / %	3.72
NiO content / wt%	2.7 (1)
Cation site 1	3*a*
x (= *y* = *z*)	0
Site occupancy	0.67 Mn, 0.33 Ni
U_{iso} / Å^2	0.0147 (6)
Cation site 2	3*a*
x (= *y*)	0
z	0.1735 (3)
Site occupancy	0.67 Na
U_{iso} / Å^2	0.054 (2)
Oxygen site 1	3*a*
x (= *y*)	0
z	0.3791 (2)
Site occupancy	1
Oxygen site 2	3*a*
x (= *y*)	0
z	-0.3791 (2)
Site occupancy	1

X-ray Absorption Near Edge Spectroscopy (XANES)

XANES spectra were collected on the Mn and Ni K-edges for selected specimens prepared using dextran biotemplating with final heating at 550 (2 h, 5 h, 12 h), 650, 750 and 850 °C (all 12 h), and for the specimen prepared via solid state (850 °C, 12 h).

Mn K-edge spectra are presented in Figure 4. For Mn, the number and position of peaks in the pre-edge region, as described by Chalmin *et al.*,[29] in combination with the peaks observed in the first derivative of the spectra gives a good indication of the oxidation state present. Using this method, all specimens made here, regardless of synthesis time and/or temperature, matched best against the Mn^{4+} standard, MnO_2; *e.g.* pre-edge features were observed at ~6540.1 and ~6542.1 eV for the MnO_2 standard and for all specimens, but not for other Mn standard materials with different oxidation states. No changes were observed with synthesis time and/or temperature in Mn K-edge position (E_0), the number and/or position of pre-edge features, or in first derivative plots. Spectra extending into the EXAFS region display no obvious variations in oscillations. It can be assumed, therefore, that Mn is tetravalent and likely in the same coordination environment in all specimens, regardless of synthetic approach.

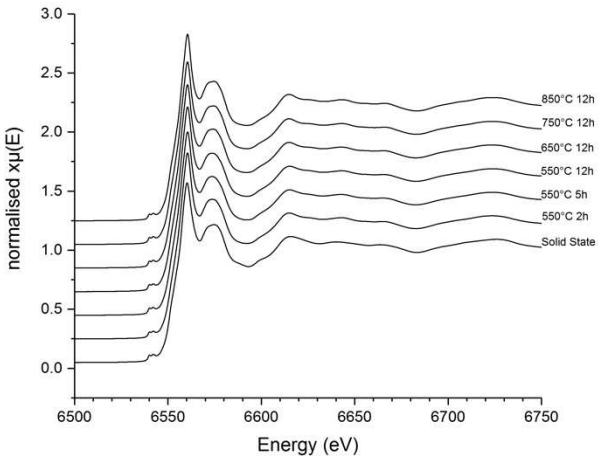

Figure 4. Mn K-edge XANES spectra for $Na_{2/3}Ni_{1/3}Mn_{2/3}O_2$ prepared by solid state synthesis at 850 °C, 12 h and *via* dextran biotemplating at 550 °C for 2, 5 and 12 h, and 650 °C, 750 °C and 850 °C for 12 h.

Similar arguments can also be made for the Ni K-edge spectra, Figure 5, which showed excellent matches in the position of a pre-edge feature at 8332.98 eV for the Ni^{2+} reference material, NiO, and all of our specimens. This feature was absent in data for Ni^0 metal foil. Again, there was no shift in edge position, E_0, nor this pre-edge feature in any of our specimens and data into the EXAFS region appear very similar regardless of synthetic approach. Ni is in the same oxidation state, likely 2+, and coordination environment in all specimens, therefore, though collection of data from reference standards in other oxidation states would fully confirm this.

There is no evidence that burning off the dextran causes a reducing effect during the early stages of synthesis leading to oxygen deficient products. From these XANES analyses, it appears that if reduction does occur then even short reaction times at higher temperatures are sufficient for both complete

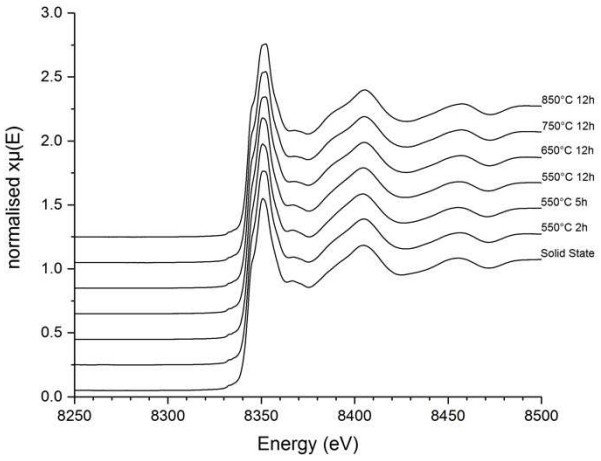

Figure 5. Ni K-edge XANES spectra for $Na_{2/3}Mn_{2/3}Ni_{1/3}O_2$ prepared by solid state synthesis at 850 °C, 12 h and via dextran biotemplating at 550 °C for 2, 5 and 12 h, and 650 °C, 750 °C and 850 °C for 12 h.

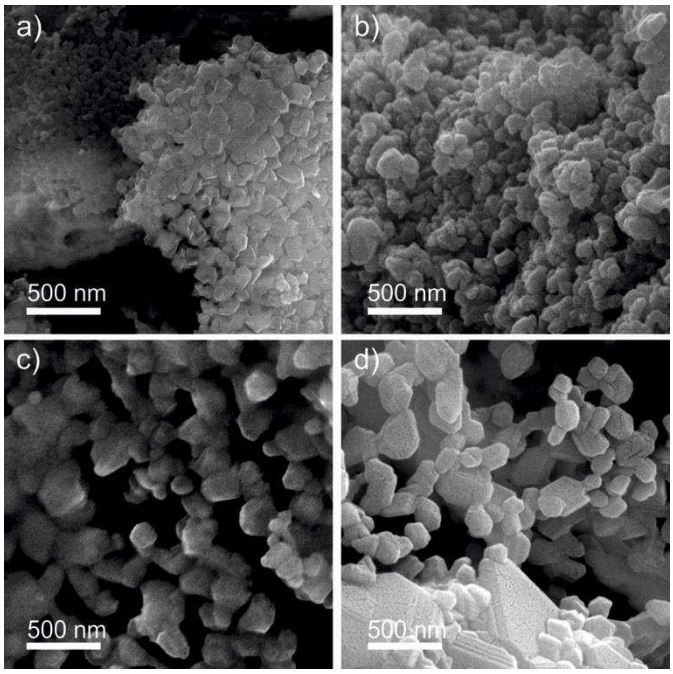

Figure 6. SEM images of $Na_{2/3}Ni_{1/3}Mn_{2/3}O_2$ powders prepared via dextran biotemplating and calcined for 2 h at (a) 550 °C, (b) 650 °C, (c) 750 °C, and (d) 850 °C

reaction and post-annealing to achieve full oxygenation.

Particle Morphology

SEM was used to examine crystal size and morphology. Figure 6 shows evolution of crystallite size with a 2 h hold by increasing temperature from 550 °C to 850 °C in the biotemplated sample, Figure 7 shows the same progression with a 12 h hold (Figure 7a-d), and the 850 °C solid state sample for comparison (Figure 7e-f). In both cases, the crystallites increase in size with increasing temperature, as would be expected from normal crystal growth. At the lower temperatures, there is little change in morphology other than size, however as the temperature is increased above 750 °C, flat, plate-like crystallites form in the dextran-templated samples, quite distinct from the morphologies observed in the solid state sample, which is particularly apparent when comparing the solid state samples (Figure 7e-f) and the biotemplated sample calcined under the same conditions (Figure 7d). The formation of plates as a direct result of the presence of the dextran indicates that the template is causing particular crystallographic faces to be over-expressed, creating a preferred orientation. This preferred orientation was also observed in the XRD and refinements, which indicated an over-expression of (00l)-type faces, as has been observed in other sodium+template systems such as sodium alginate,[30] although this is first time that such plate-like morphologies have been observed without the use of a sodium alginate template,[30] indicating that the interaction of the sodium and glycosidic ring structures may be the driver for morphology as these are the main commonalities between the systems. The wider implications the appearance of this morphology are therefore currently under further investigation.

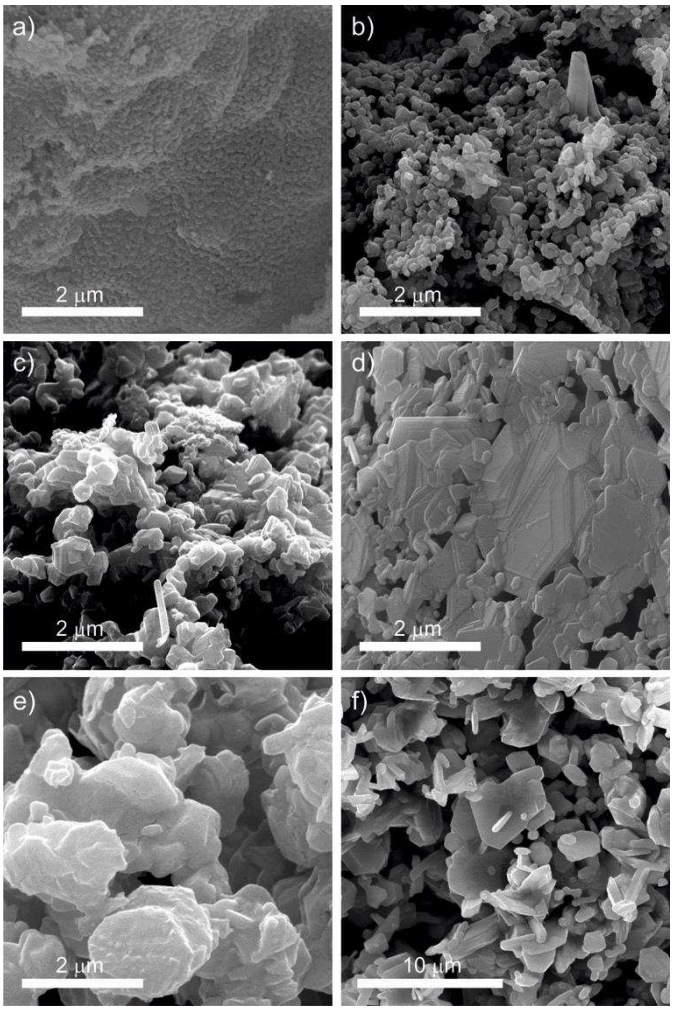

Figure 7. SEM images of $Na_{2/3}Ni_{1/3}Mn_{2/3}O_2$ powders prepared via dextran biotemplating and calcined for 12 h at (a) 550 °C, (b) 650 °C, (c) 750 °C, and (d) 850 °C. Images (e-f) are from powders made via solid state synthesis at 850 °C, 12 h, with two different levels of magnification.

Figure 8 shows evolution of crystallite size with time held at 650 °C, and again shows the expected increase in crystallite size with increasing time. The crystallite size evolution for all samples is shown in Table 1. Of particular note is the difference between the average crystallite size in solid state and biotemplated samples, whether synthesised under equivalent conditions (850 °C, 12 h, 1740 ± 742 nm and 553 ± 253 nm respectively), or at lower temperatures/times, demonstrating the precision with which biotemplating can be used to target crystallite size.

The BET surface area was determined using nitrogen

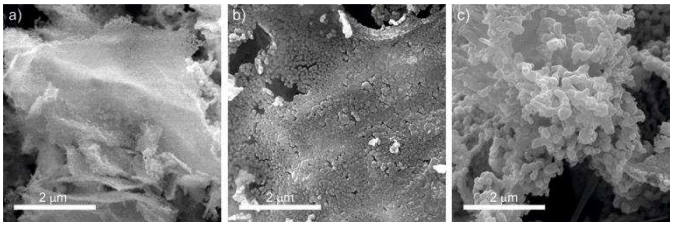

Figure 8. SEM images of $Na_{2/3}Ni_{1/3}Mn_{2/3}O_2$ powders prepared via dextran biotemplating and calcined at 650 °C for (a) 2 h, (b) 5 h and (c) 12 h.

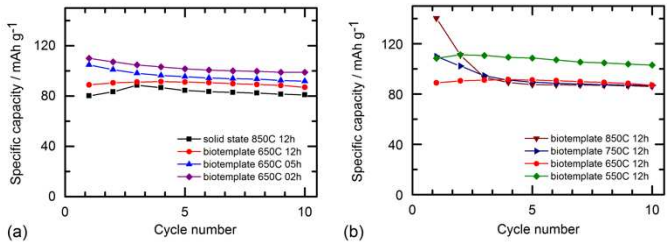

Figure 9 Specific discharge capacities versus cycle number for (a) solid state and biotemplated $Na_{2/3}Ni_{1/3}Mn_{2/3}O_2$ calcined at 650 °C for 2 h, 5 h and 12 h and (b) biotemplated $Na_{2/3}Ni_{1/3}Mn_{2/3}O_2$ calcined at for 12 h at 850 °C, 750 °C, 650 °C and 550 °C.

sorption, with results listed in Table 1. The data follow the same trends as the particle size analysis and indicate that there is a significant change in the nature of the samples between either 550 °C and 650 °C, or 550 °C for 5 h and 12 h, where a large decrease in surface area is observed. This suggests that there has not been a full transition from organic/inorganic composite to crystalline product, which may impair electrochemical behaviour.

Electrochemistry

The electrochemical performance of NNM produced using biotemplating with various reaction time/temperature combinations was tested alongside that of material made via solid state reaction. Cells were tested over 10 charge-discharge cycles between 2.0 - 4.2 V to study how the control of particle size and surface area permitted by biotemplating might impact on the electrochemical properties of NNM. Table 1 collates values of initial charge and discharge capacities (q_{c1} and q_{d1}, respectively), first cycle coulombic efficiency, $C.E._1$, and tenth discharge capacity, q_{d10} for each specimen.

Cycling Performance

Cells containing NNM produced via solid state reaction gave initial discharge capacity, Figure 9a, of 80.1 mAh g^{-1}, indicating the reversible (de)intercalation of roughly half of the initial sodium content. This capacity is typical for NNM cycled between 2.0 - 4.2 V, [9,10,31] and is stable over ten cycles.

Biotemplated materials display significantly higher specific discharge capacity, q_{d1}, than the solid state material, Table 1, and this improved performance is retained on cycling. A likely major contributing factor is the large difference in average particle size between solid state (1740 nm) and biotemplated materials (115 - 167 nm), with significantly reduced diffusion lengths enabling effective utilization of more electrode material. The polymorphic change from predominantly P2-NNM in the solid state sample to P3-NNM in all biotemplated materials may also play a role, though there have been no reports of high specific capacities for P3-NNM to date.[10]

For biotemplated materials calcined at 650 °C, it is evident, Figure 9a, that correlations exist between the duration of calcination and reversible capacity; specifically, increasing the length of thermal treatment results in reduced capacities, with first discharge capacities of 110 mAh g^{-1} for the material calcined for 2 h, 104.8 mAh g^{-1} for 5 h, and 88.8 mAh g^{-1} for 12 h. These values are significantly larger than seen for the solid state material. This relationship is maintained on cycling, with 98.9 mAh g^{-1} being delivered by the biotemplated material calcined at 650 °C for 12 h after 10 cycles, compared with 81.0 mAh g^{-1} from the solid state material.

Figure 9b illustrates the specific discharge capacity of biotemplated materials that were calcined at various temperatures for 12 hours. Biotemplated materials calcined at 750 °C and 850 °C show high initial specific capacities, which rapidly converge to *ca.* 87 mAh g^{-1}, possibly indicative of structural changes within the first few cycles. Materials calcined at 550 °C and 650 °C show better capacity retention on cycling, with the sample heated at 550 °C, 12 h, showing both good initial specific discharge capacity (108.5 mAh g^{-1}) and good capacity retention after ten cycles, at 103.1 mAh g^{-1}. This variation is likely due to changes in average particle sizes.

Cells assembled using biotemplated materials calcined at 550 °C for 2 and 5 h did not cycle reliably, with little or no reversible capacity observed. The large specific surface areas, Table 1, of these materials may have resulted in excessive electrolyte degradation during charge. This suggests there may be optimal values for both particle size and surface area which lead to improved electrochemical performance, and that the control of these parameters permitted by biotemplating may be advantageous in such optimisation.

Electrochemical Behaviour

(Dis)charge profiles recorded at 10 mA g^{-1} for the initial cycle of a cell using NNM produced using solid state reactions are shown in Figure 10a; the step-like nature of the profiles are typical for P2-NNM materials cycled between 2.0 - 4.2 V.[32–34] Biotemplated materials follow the same profile through the first charge plateau at ~3.3 V but diverge as the capacity exceeds *ca.* 60 mAh g^{-1}. The solid state material goes through two further charge plateaus before rising quickly to the cut-off potential, whilst all biotemplated specimens exhibit a second plateau (*ca*. 3.6 V) and gradually increase through a less discrete third charge plateau to the cut-off potential. Discharge curves are broadly similar, with biotemplated samples producing greater specific capacities and slightly different behaviour at cut off potentials; the solid state material exhibits little discharge capacity above 3.5V.

Structural transitions associated with intercalation processes can be identified from plateaus present in voltage-capacity profiles, which become more apparent in plots of differential capacity and potential; initial cycles from Figure 10a are represented this way in Figure 10b. For the solid state material, distinct peaks occur at 3.21, 3.29, 3.64 and 4.07 V during charge, and at 3.54, 3.20 and 3.13 V on discharge. This compares favourably with behaviour reported for P2-NNM,[28] though there is a notable absence of any significant charging peak at *ca.* 3.7 V.

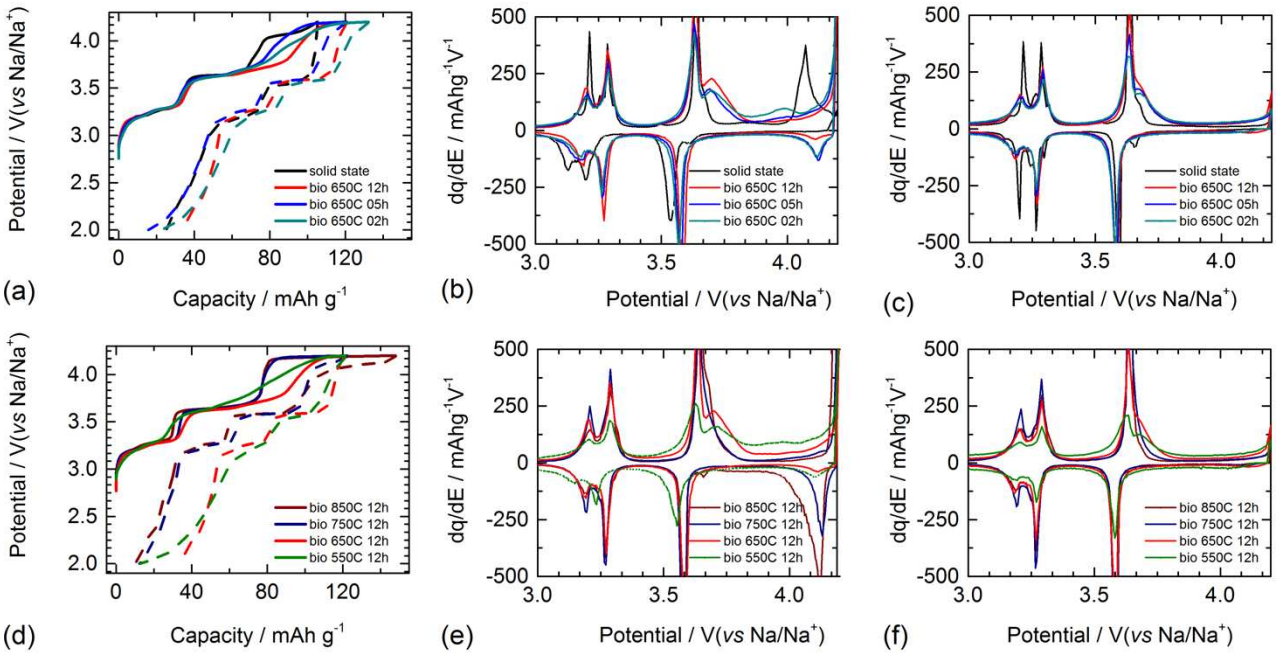

Figure 10 (a) Voltage profiles of the first galvanostatic charge and discharge (dashed line) of solid state and biotemplated $Na_{2/3}Ni_{1/3}Mn_{2/3}O_2$ calcined at 650 °C for 2 h, 5 h and 12h, (b) differential capacity plots for the initial charge-discharge cycle for the samples illustrated in (a), (c) differential capacity plots for the tenth charge-discharge cycle for the samples illustrated in (a), (d) Voltage profiles of the first galvanostatic charge and discharge (dashed line) of biotemplated $Na_{2/3}Ni_{1/3}Mn_{2/3}O_2$ calcined at for 12 h at 850 °C, 750 °C, 650 °C and 550 °C (e) differential capacity plots for the initial charge-discharge cycle for the samples illustrated in (d),and (f) differential capacity plots for the tenth charge-discharge cycle for the samples illustrated in (a). Materials were cycled in half-cells between 2.0 and 4.2 V (vs Na/Na+) at 10 mA g^{-1} and 25 °C.

Differential capacity profiles for biotemplated materials, Figure 10b, correlate well with reported cyclic voltammograms for P3-NNM over the 3.0 - 4.0 V range.[10] The most apparent differences exhibited by the biotemplated specimens during the first cycle, when compared against the solid state sample, are: (i) an additional charging peak at 3.70 V, (ii) the absence of a charging peak at 4.07 V, (iii) discharge peaks shifted to higher potentials, and (iv) a significant discharge peak at 4.12 V. It can also be seen that the capacity associated with the charging process at 3.70 V increases with calcination time.

Figure 10d shows the results obtained from cycling biotemplated materials calcined for 12h at 850 °C, 750 °C, 650 °C or 550 °C. Charge-discharge profiles are similar to the biotemplated materials in Figure 10a, though materials calcined at 750 °C and 850 °C display a distinct charge step at a capacity of *ca.* 80 mAh g^{-1}, corresponding closely to the behaviour of the solid state material (*i.e.* P2-type). The largest charge passed during first cycle is associated with the biotemplated material calcined at 850 °C, 12 h. From Figure 10e, the region that relates to this material's excess capacity is at the top of charge (4.20 V), with a corresponding discharge peak at ~4.10 V decreasing in significance with decreasing calcination temperature. Peaks at 3.64 V on charge and 3.58 V on discharge also become less pronounced with decreasing calcination temperature. The improved capacity diminishes on cycling, indicating irreversible changes occur during the first few cycles.

Substantially different behaviour is seen for biotemplated material calcined at 550 °C, 12 h, which exhibits the smoothest charge profile, Figure 10d, and significant capacity at potentials below 3.0 V. This material shows a high degree of reversibility, retaining 103.1 mAh g^{-1} after ten cycles. This behaviour is similar to that of the solid state material; when comparing Figures 10b and 10e, both materials exhibit peaks at the same voltages during charge and discharge. Moreover, these materials retain the highest proportion of their initial discharge capacity and show the least variation in differential capacity after ten cycles, Figures 10c and 10f.

For biotemplated materials calcined for varying times at 650 °C, Figure 10c, the small discharge peak at 4.10 V in the initial cycle becomes insignificant after ten cycles. Similar behaviour is seen for templated specimens calcined for 12 h at different temperatures, Figure 10f. Also, discharge peaks from the initial discharge of solid state materials at potentials of 3.20 and 3.13 V shift to 3.27 V and 3.20 V, overlapping with the curves of the biotemplated materials. This convergent behaviour in charge and discharge profiles on cycling suggests the formation of a particular structure is favoured by these materials after a few charge-discharge cycles. Notably, the biotemplated material calcined at 550 °C for 12 h does not follow this trend and on cycling retains the original peak positions of the initial cycle (at slightly lower potentials than the other materials) and a high degree of discharge capacity.

When comparing behaviours illustrated in Figure 10e, it is apparent that the significance of the charging peak at 3.64 V diminishes with decreasing calcination temperature. Coupled with the behaviour seen at this potential in Figure 10b, it can be inferred that the presence of this peak indicates that a series of structural changes occur during calcination. As this

peak is not present for the solid state material, this behaviour is likely specific to the P3-phase.

In summary, the best performing cells were those containing biotemplated material calcined at 550 °C for 12 h. This is likely due to two factors: the polymorph produced (P3), and reduced particle size. The lower temperatures and shorter heating times used by the biotemplating method offers the possibility to reduce energy consumption and associated environmental and economic costs during production, whilst simultaneously producing a tailorable product as a route to improved electrochemical performance.

Conclusions

We have presented a new sustainable synthetic method for the preparation of energy storage materials, which allows a high level of selectivity in the size of crystallites formed. Specifically, dextran biotemplating shows control of particle morphology and phase formation in $Na_{2/3}Ni_{1/3}Mn_{2/3}O_2$, NNM. High purity NNM materials were prepared in the less-commonly reported P3 polymorph using this new approach, with average crystallite sizes varying from ~100 - 550 nm purely as a function of calcination temperature and time.

The dextran template produced plate-like crystallites, with (00l) faces overexpressed, at higher temperatures and work is ongoing to elucidate the main mechanisms which drive this. Every dextran-templated sample prepared showed higher specific capacities than an equivalent made *via* traditional solid state reaction; the best performance was observed for a biotemplated sample made at 550 °C for 12 h, which showed a large and significant improvement over the solid state, 103.1 $mAhg^{-1}$ *vs* 80.1 mAh g^{-1} after 10 cycles.

This work shows that biotemplating can be successfully applied to energy storage materials with tailorable particle morphologies over nano- and micron-scales, reducing energy intensive synthetic processes while delivering improved electrochemical performance. Biotemplating has the potential to enable the development of previously overlooked functional materials.

Conflicts of interest

There are no conflicts to declare.

Acknowledgements

This research was performed in part at the MIDAS Facility, at the University of Sheffield, which was established with support from the Department of Energy and Climate Change. We thank Diamond Light Source for the award of beam time as part of the Energy Materials Block Allocation Group **SP14239**, and Giannantonio Cibin for collection of the hard XAS data. RB acknowledges that this project was supported by the Lloyd's Register Foundation and Royal Academy of Engineering under the Research Fellowships scheme.

References

1 J. S. Kim, D. Y. Kim, G. B. Cho, T. H. Nam, K. W. Kim, H. S. Ryu, J. H. Ahn and H. J. Ahn, *J. Power Sources*, 2009, **189**, 864–868.
2 M. Nishijima, I. D. Gocheva, S. Okada, T. Doi, J. ichi Yamaki and T. Nishida, *J. Power Sources*, 2009, **190**, 558–562.
3 P. Moreau, D. Guyomard, J. Gaubicher and F. Boucher, *Chem. Mater.*, 2010, **22**, 4126–4128.
4 J. Barker, M. Y. Saidi and J. L. Swoyer, *Electrochem. Solid-State Lett.* , 2003, **6**, A1–A4.
5 K. T. Lee, T. N. Ramesh, F. Nan, G. Botton and L. F. Nazar, *Chem. Mater.*, 2011, **23**, 3593–3600.
6 R. Tripathi, T. N. Ramesh, B. L. Ellis and L. F. Nazar, *Angew. Chemie - Int. Ed.*, 2010, **49**, 8738–8742.
7 J. Paulsen and J. Dahn, *Solid State Ionics*, 1999, **126**, 3–24.
8 H. Wang, B. Yang, X. Z. Liao, J. Xu, D. Yang, Y. S. He and Z. F. Ma, *Electrochim. Acta*, 2013, **113**, 200–204.
9 G. Liu, L. Wen, Y. Li and Y. Kou, *Ionics (Kiel).*, 2015, **21**, 1011–1016.
10 S. Y. Lee, J. H. Kim and Y. C. Kang, *Electrochim. Acta*, 2017, **225**, 86–92.
11 C. Delmas, C. Fouassier and P. Hagenmuller, *Phys. BC*, 1980, **99**, 81–85.
12 M. Keller, D. Buchholz and S. Passerini, *Adv. Energy Mater.*, 2016, **6**, 1–11.
13 S. Komaba, N. Yabuuchi, T. Nakayama, A. Ogata, T. Ishikawa and I. Nakai, *Inorg. Chem.*, 2012, **51**, 6211–6220.
14 S. Guo, P. Liu, H. Yu, Y. Zhu, M. Chen, M. Ishida and H. Zhou, *Angew. Chemie Int. Ed.*, 2015, **54**, 5894–5899.
15 W. Zhao, H. Kirie, A. Tanaka, M. Unno, S. Yamamoto and H. Noguchi, *Mater. Lett.*, 2014, **135**, 131–134.
16 Z. Y. Li, J. Zhang, R. Gao, H. Zhang, Z. Hu and X. Liu, *ACS Appl. Mater. Interfaces*, 2016, **8**, 15439–15448.
17 A. Jaiswal, C. R. Horne, O. Chang, W. Zhang, W. Kong, E. Wang, T. Chern and M. M. Doeff, *J. Electrochem. Soc.*, 2009, **156**, A1041.
18 D. Larcher and J.-M. Tarascon, *Nat. Chem.*, 2015, **7**, 19–29.
19 Z. Schnepp, *Angew. Chemie - Int. Ed.*, 2013, **52**, 1096–1108.
20 D. Walsh, L. Arcelli, T. Ikoma, J. Tanaka and S. Mann, *Nat. Mater.*, 2003, **2**, 386–390.
21 R. Boston, A. Carrington, D. Walsh and S. R. Hall, *CrystEngComm*, 2013, **15**, 3763.
22 D. Walsh, S. C. Wimbush and S. R. Hall, *Chem. Mater.*, 2007, **19**, 647–649.
23 B. H. Toby, *J. Appl. Crystallogr.*, 2001, **34**, 210–213.
24 Larson A. C. and R. B. Von Dreele, *General Structure Analysis System (GSAS) Los Alamos National Laboratory Report*, 2000.
25 A. J. Dent, G. Cibin, S. Ramos, A. D. Smith, S. M. Scott, L. Varandas, M. R. Pearson, N. A. Krumpa, C. P. Jones and P. E. Robbins, *J. Phys. Conf. Ser.*, 2009, **190**, 12039.
26 B. Ravel and M. Newville, *J. Synchrotron Radiat.*, 2005, **12**, 537–541.
27 J. Schindelin, C. T. Rueden, M. C. Hiner and K. W. Eliceiri, *Mol. Reprod. Dev.*, 2015, **82**, 518–529.
28 Z. Lu and J. R. Dahn, *J. Electrochem. Soc.*, 2001, **148**, A1225.

29 E. Chalmin, F. Farges and G. E. Brown, *Contrib. to Mineral. Petrol.*, 2009, **157**, 111–126.
30 Z. A. C. Schnepp, S. C. Wimbush, S. Mann and S. R. Hall, *Adv. Mater.*, 2008, **20**, 1782–1786.
31 P. F. Wang, H. R. Yao, X. Y. Liu, J. N. Zhang, L. Gu, X. Q. Yu, Y. X. Yin and Y. G. Guo, *Adv. Mater.*, 2017, **29**, 1–7.
32 R. Fielden and M. N. Obrovac, *J. Electrochem. Soc.*, 2015, **162**, A453–A459.
33 J. Molenda, *Solid State Ionics*, 1986, **21**, 263–272.
34 D. H. Lee, J. Xu and Y. S. Meng, *Phys. Chem. Chem. Phys.*, 2013, **15**, 3304.